5-3. Contract Beamlines

BL22XU
JAEA Actinide Science I

1. Introduction

BL22XU is designed to promote basic and applied research on (1) actinide chemistry, (2) energy and environmental materials, (3) Fukushima environmental recovery and decommissioning, and related research [1]. It was constructed in the Storage Ring and the RI Laboratory of SPring-8 to investigate radioactive materials containing sealed transuranium elements and nuclear fuel materials. In January 2024, dust samples from the operations floor of the Fukushima Daiichi Nuclear Power Plant are scheduled to be measured by XRF, XAFS, XRD, etc.

BL22XU has two double-crystal monochromators. One is a single-cam-type monochromator with a multicrystal switching system. This monochromator can utilize wide-energy-range X-rays from 4 to 72 keV by using Si(111) and Si(311) crystals. The other is a calculation-and-combination-type monochromator. This monochromator can utilize high-flux X-rays from 35 to 70 keV by using Si(111) crystals.

BL22XU has mirrors for focusing and higher harmonics rejection. They focus X-rays of 1 mm height and 3 mm width to 0.2 mm and 0.4 mm, respectively, in the RI Laboratory at 120 m from the light source. The three mirrors are switched to reject harmonics higher than 7, 16, and 30 keV. A beryllium diffraction lens system for the higher energy and a Kirkpatrick–Baez (KB) micro-focusing system for less than 40 keV are also used.

2. Experimental hutch 1 (EH1)

2-1. Large diffractometer

Currently, an apparatus for Bragg coherent X-ray diffraction imaging (Bragg-CDI) is under development. Bragg-CDI is expected to be a powerful technique for investigating isolated nanosized crystalline particles. Furthermore, it is expected to enable studies of particles located within devices, which are inaccessible by electron beam techniques. This technique is now applicable to study particles from 40 to 1000 nm in size and from room temperature to 1373 K.

In 2022, the Bragg-CDI contributed to the development of negative thermal expansion (NTE) materials with 11.1% volume shrinkage [2]. The complementary use of a transmission electron microscope and Bragg-CDI have revealed the phase coexistence of cubic and tetragonal phases with a large volume difference. It was suggested that the change in the hetero-phase structure dominates the NTE character.

We also have succeeded in visualizing a 500 nm single grain of $BaTiO_3$ in polycrystalline ceramics [3]. The lattice strain distribution of grains in the paraelectric phase and a pair of 90° domains of the ferroelectric phase were imaged in three dimensions. These results suggest that the domain boundaries correlate with the strain induced by stress from adjacent grains.

2-2. Diamond-anvil-cell diffractometer

The diamond-anvil-cell diffractometer is designed

for both single-crystal and powder X-ray diffraction experiments under high pressure and low temperature. It is equipped with large-area two-dimensional detectors that cover a wide diffraction angle. By using these detectors and high-energy monochromatic X-rays of up to 70 keV, this diffractometer enables us to measure the X-ray total scattering pattern even in a high-Q range with a short exposure time. The measured X-ray total scattering pattern transforms into a pair-distribution function (PDF).

The PDF profile corresponds to the probability of finding atom pairs at a distance in real space, so the PDF analysis is one of the powerful methods to analyze the local structure at the scale of sub-nanometers to several nanometers. The structural information of functional materials in local to middle-range structures has been regarded as important for understanding their properties. Our rapid-acquisition PDF measurement system has been applied to a wide variety of functional materials, such as battery (electrode) materials [4], hydrogen-absorbing materials [5], and cement materials [6]. The PDF measurements of the sodium-containing layered manganese-nickel oxides, which are electrode materials for sodium-ion batteries, have helped us to discover that lowering the crystallinity of the layered oxide improves the charge–discharge properties [4].

3. Experimental hutch 3 (EH3)

3-1. Hard X-ray photoemission spectroscopy (HAXPES)

The development of the device is underway to realize direct power generation from gamma rays. A SiC device with high radiation tolerance is proposed as a candidate.

The interface states of Ni/SiC with different electrical properties were investigated by HAXPES. Figure 1 shows HAXtoseES spectra of Ni $2p_{3/2}$ near the binding energy (BE) region. In the spectrum of sample 20, the BE of Ni $2p_{3/2}$ has a well-matched peak position to that of the BE of the metallic Ni. Thus, during the fabrication of the Ni/SiC Schottky junction, Ni remains mainly in the metallic state. On the other hand, in the spectrum of sample 22, the BE is clearly shifted to the higher energy side by ~0.8 eV compared with the BE of Ni metal. Judging from the peak position, it is possible that Ni_2Si (BE=853.3 eV) [7] was formed at the interface during junction fabrication.

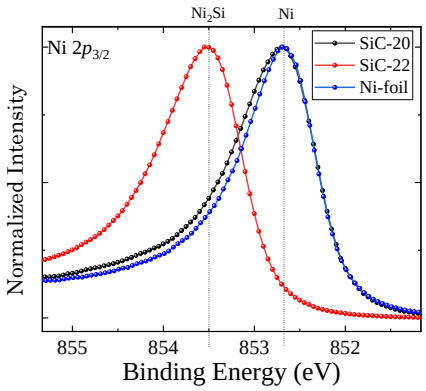

Fig. 1. HAXPES spectra near the Ni $2p_{3/2}$ region for Ni/SiC samples 20 (black) and 22 (red), as well as Ni foil (blue) as the standard reference.

HAXPES measurements suggest that Ni-Si compounds are formed at the interface in samples with large ideality factors, which may directly affect the energy conversion efficiency. Therefore, imperfect Schottky junctions may be the cause of the performance degradation [8]. In future studies, the performance will be compared with thoseof other types of junctions, such as *pn* junctions. We

note that the evaluation of interface conditions by HAXPES may provide information on sample quality that cannot be obtained by *I–V* measurements alone.

3-2. X-ray absorption fine structure (XAFS)

(1) Research on separation and recovery of rare metals from spent products

Taking advantage of the high-brilliance XAFS (X-ray absorption fine structure) measurement system using an undulator synchrotron radiation, we have been studying the separation and recovery of rare metals from urban mines.

Palladium, a member of the platinum group, is an essential metal in the manufacture of catalysts for automobile exhaust systems and medical products. Russia and the Republic of South Africa account for more than 80% of the world's palladium production (2017). However, repeated closures of platinum mines in South Africa and international conflicts in Russia have caused prices to soar. Therefore, efficient metal recycling is becoming increasingly important. HNO_3 leaching is used to recycle spent Pd products used as dental materials, but in leaching, low concentrations of Pd(II) dissolve in the Ag(I) solution. Therefore, we aimed to selectively adsorb and recover Pd(II) from dental materials such as Ag(I), Cu(II), NI(II), and Fe(III).

To separate Pd(II) from Ag(I), we focused on *N*-donor-type adsorbents with harder and softer basicity than those of the sulfide- and oxygen-based adsorbents, respectively. In this study, we investigated the fundamental adsorption properties and separability of Pd(II) and Ag(I) in HNO_3 solutions using adsorbents (Fig. 2) bearing amine (**R-Amine**), pyridine (**R-Py**), iminodiacetic acid, (**R-IDA**) or bis-picolylamine (**R-BPA**) functional groups. The adsorption mechanisms were investigated via metal separation studies, Fourier transform infrared (FT-IR) spectroscopy, and X-ray absorption fine structure (XAFS) spectroscopy [9].

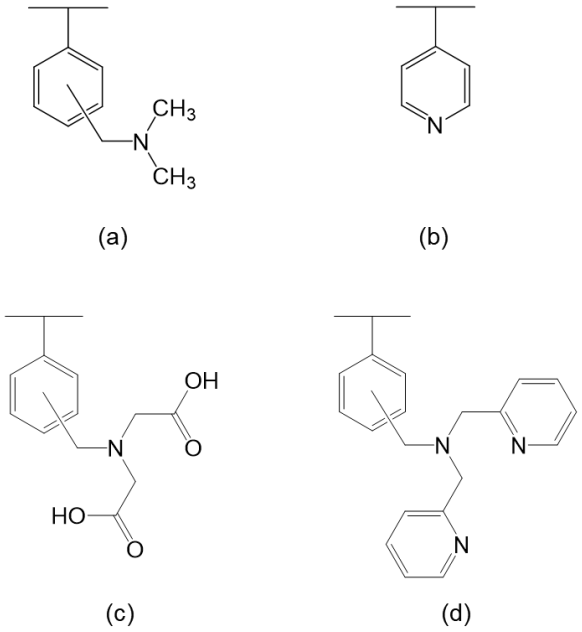

Fig. 2. Structures of the functional groups on the adsorbents: (a) R-Amine, (b) R-Py, (c) R-IDA, and (d) R-BPA.

(2) XAFS analysis for hybrid-waste-solidification of mobile nuclei

Regarding the Fukushima-Daiichi Nuclear Power Plant (1F) accident, stable solidification and disposal of secondary waste generated in the treatment of contaminated water have become important issues. Thus, we focused on iodine, which is the predominant element of long-term exposure dose owing to its long half-life and low adsorptivity, and minor actinides, which are potentially hazardous owing to their long half-life alpha radioactivity, and investigated a new solidification method in which the primary waste is enclosed in metal or ceramic materials and fixed by spark

plasma sintering (SPS) or hot isostatic pressing (HIP) methods. In this study, to discuss the stability and reactivity of the solidified samples, the chemical states and local structures of the contained elements were investigated by the XAFS method.

Figure 3 shows the results of mapping the distributions of I and Ag using the KB micro-focusing system and silicon drift detector (SDD) for a sample of AgI as a primary waste mixed with Zr as a matrix material and solidified by the HIP method. This result indicates that I is widely distributed but Ag is localized into clusters.

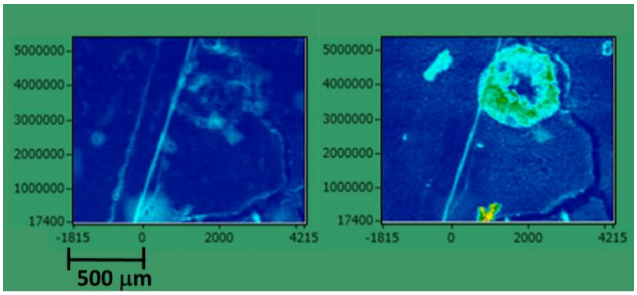

Fig. 3. Elemental mapping of solidified AgI/Zr showing I (left) and Ag (right).

Thus, I and Ag K-edge XAFS spectra were measured at the characteristic positions by using the focusing system and QXAFS system (Fig. 4). As a result, it was found that I existed as I^- regardless of the position, but some Ag was reduced from Ag^+ to Ag^0. In particular, a large amount of reduced Ag is observed near the boundary between the Ag cluster and the matrix material. In addition, Zr K-edge XAFS results revealed that Zr, the matrix material, was oxidized where Ag was largely reduced. These results suggest that Ag, which is highly reactive, is strongly fixed in the Zr matrix, while I, which is less reactive, tends to diffuse during the solidification process.

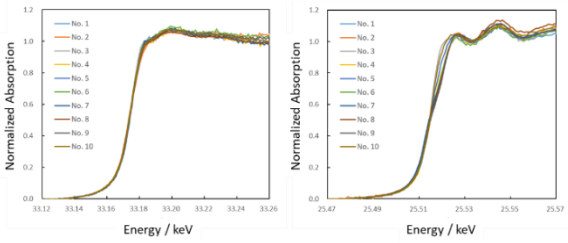

Fig. 4. I K-edge (left) and Ag K-edge (right) XAFS spectra of solidified AgI/Zr measured at several different sample positions.

Such knowledge will be very useful information for selecting a safe and effective solidification method.

3-3. Stress/imaging measurements

In this device, deformation and state changes inside a material are determined by a diffraction method and an imaging method using high-energy synchrotron radiation X-rays. Figure 5 shows the time dependence of the internal temperature and the change in the radial stress $\Delta\sigma_z$ at a point 2.1 mm away from the surface of the 18650-type lithium-ion battery (LIB), as well as the surface temperature measured using the thermocouple and the voltage and current during battery operation. In the case of the 1C charge process, $\Delta\sigma_z = -31$ MPa, because in the charge process, owing to the anode expansion caused by lithium intercalation, $\Delta\sigma_z$ of the Cu anode collector decreases (compression). In the case of the 1C discharge process, $\Delta\sigma_z$ increased by 44 MPa (tensile) from the end of the 1C charge process owing to anode contraction. Moreover, the internal temperature at the point 2.1 mm away from the surface agreed with the surface temperature. In the case of the 2C cycle, $\Delta\sigma_z$ decreased by 15–43 MPa in the last charge process, as represented by dashed lines in Fig. 5; this shows a similar change to that in

the 1C charge process. The surface and internal temperatures increased during the last discharge process. Moreover, the internal temperature was reasonably higher (by ~4 °C) than the surface temperature. In the case of the 3C cycle, the surface temperature rose from 29 to 47 °C, and the internal temperature was higher by ~6 °C than the surface temperature. $\Delta\sigma_z$ decreased by 47 MPa during the 3C cycle from the start of the 3C operation.

Thus, the operando measurement is expected to clarify the degradation mechanism in LIBs for electric vehicles during the charge–discharge cycles by measuring the internal temperature and stress distribution from the center to the surface [10].

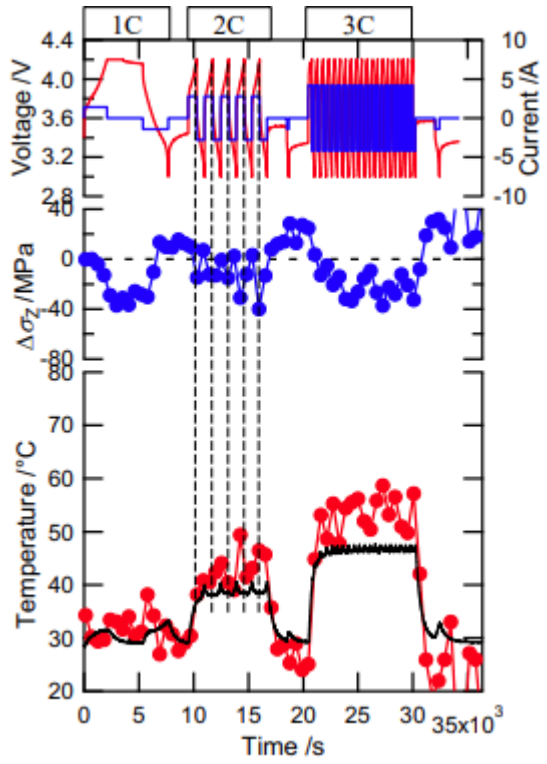

Fig. 5. Time dependence of internal and surface temperatures, change of stress ($\Delta\sigma_z$) in the 18650-type LIB, and voltage and current during the charge–discharge cycles.

3-4. κ-type diffractometer

(1) Pair distribution function (PDF) analysis

The current amplifier used as the I_0 monitor in the data collection for PDF analysis was updated. The new current amplifier is more stable and has an improved signal-to-noise ratio owing to the reduced variation of dark current. This enabled us to extract the local structure of two-component systems in PDF analysis and to obtain the nearest-neighbor interatomic distances of light elements.

The results obtained from the local structure analysis using the PDF of the solid solution of DyN and diluent ZrN, a nitride simulated fuel, are shown below.

DyN and ZrN are metal nitrides with a NaCl-type structure and are in total solid solution; the crystallinities of DyN and ZrN are very different, and that of DyN is not as good as that of ZrN. EXAFS measurements show that there is only one bond distance between the metal and nitrogen in ZrN, while DyN has a long bond owing to the fact that DyN has both a long bond and a short bond, whereas ZrN has only one bond. The lattice parameter of the DyN–ZrN solid solution does not follow Vegard's law and an anomaly occurs near $Dy_{0.5}Zr_{0.5}N$.

The PDF analysis shows that Dy and Zr form a superlattice structure ordered by Dy and Zr near $Dy_{0.5}Zr_{0.5}N$. In addition to the PDF and Lee and Belt analyses, the results obtained from EXAFS measured at the Dy-K and Zr-K absorption edges are summarized in Fig. 6 [11]. The local structures obtained from the PDF and EXAFS are in good agreement, but deviations from the average structure obtained from Rietveld analysis are observed.

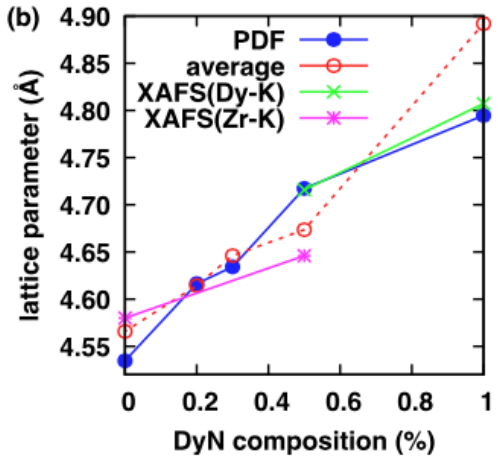

Fig. 6. Lattice parameters obtained by the Rietveld refinement and calculated using the nearest-neighbor bond distance obtained by the PDF and XAFS.

(2) Surface structure diffractometer

Studies of various electrolyte/electrode interfaces were carried out using a κ-type multi-axis diffractometer. The interface structure of the all-solid-state LIB electrode during charge/discharge cycles, the interface structure of the electrocatalysis electrodes, and the electrode surface structure during the underpotential deposition (UPD) reaction of Bi in an ionic liquid (IL) were studied. Here, we report the study of the Au(111) electrode surface structure in 1-butyl-3-methylimidazolium tetrafluoroborate ([BMIM]BF4) under potential control using the surface X-ray scattering (SXS) technique. Previously, we found that the UPD reaction of Bi occurs in [BMIM]BF_4 and the Bi layer is a monolayer. In this study, we tried to understand why the UPD reaction occurs in [BMIM]BF_4. SXS measurements were carried out in neat [BMIM]BF_4. The results of SXS measurements showed that the (p × √3) reconstructed surface structure existed, and the surface structure reversibly changed between the (1 × 1) and (p × √3) structures depending on the electrode potential. These results indicate that the interaction between the Au(111) surface and [BMIM]BF_4 was weak, as observed in aqueous electrolytes, and the weak interaction enables electrodeposited Bi atoms to form a monolayer.

Tanida Hajime[*1], Machida Akihiko[*2], Ohwada Kenji[*2], Kobata Masaaki[*1], Fukuda Tatsuo[*1], Kobayashi Tohru[*1], Shobu Takahisa[*1], Tominaga Aki[*1], Yoneda Yasuhiro[*1], Tamura Kazuhisa[*1], Okamoto Yoshihiro[*1]

[*1]Japan Atomic Energy Agency

[*2]National Institutes for Quantum Science and Technology

References:

[1] Shiwaku, H. et al. (2023). *JAEA-Research* **2022-015**, 39.

[2] Nishikubo, T. et al. (2023). *Chem. Mater.* **35**, 870–878.

[3] Oshime, N. et al. (2023). *Jpn. J. Appl. Phys.* **62**, SM1022.

[4] Kataoka, R. et al. (2023). *Batteries Supercaps* **6**, e202200462.

[5] Sakaki, K. et al. (2022). *Acta Mater.* **234**, 118055.

[6] Kim, G. et al. (2022). *Cem. Concr. Res.* **159**, 106869.

[7] Tam, P. L. & Nyborg, L. (2009) *Surf. Coat. Technol.* **203**, 2886–2890.

[8] Fukuda, T. et al. (2022) *J. Appl. Phys.* **132**, 245102.

[9] Suzuki, T. et al. (2023). *Sep. Purif. Technol.* **308**, 122943–122949.

[10] Hirano, T. et al. (2023). *SPring-8/SACLA Research Report*, **11**, 49–57.

[11] Yoneda, Y. et al. (2023), *Physica B* **663**, 414960.